High-Gain Dual-Band Dual-Sense Circularly Polarized Spiral Series-Fed Patch Antenna

NGHIA NGUYEN-TRONG[1] (Member, IEEE), SHENGJIAN JAMMY CHEN[1,2] (Member, IEEE),
AND CHRISTOPHE FUMEAUX[1] (Fellow, IEEE)

[1]School of Electrical and Electronic Engnieering, University of Adelaide, Adelaide, SA 5005, Australia

[2]College of Science and Engineering, Flinders University, Adelaide, SA 5042, Australia

CORRESPONDING AUTHOR: N. NGUYEN-TRONG (e-mail: nghia.nguyentrong@adelaide.edu.au)

This article has supplementary downloadable material available at https://doi.org/10.1109/OJAP.2022.3161129, provided by the authors.

ABSTRACT This paper demonstrates a dual-band circularly polarized (CP) two-dimensional (2D) series-fed patch array antenna. The CP rotating sense in each band is opposite to each other, which makes them well-suited for the downlink and uplink in satellite applications. The antenna can be designed to achieve a very high gain with a simple feeding structure using spiral microsip line, which can be integrated on a single-layered substrate. A theoretical framework for this type of antennas has been developed, which facilitates an efficient and fast design procedure requiring minimal computational resource. A prototype has been fabricated and measured, showing operating bandwidths (overlapped 10-dB return loss, 3-dB gain, 3-dB axial ratio bandwidths) of about 7% and 5%, realized broadside gains of 21.5 and 22 dBic at 12 and 14 GHz bands, respectively. This is an outstanding performance considering that the antenna profile is only 0.03 free-space wavelength (at 12 GHz) and the ratio between two operating frequencies is very tight accounting to only 1.17.

INDEX TERMS Antenna array, Archimedean spiral, circular polarization, high gain, leaky-wave antenna, microstrip patch antenna, series-fed patch antenna, satellite communications.

I. INTRODUCTION

SATELLITE communications require significantly high antenna gain with circular polarization (CP). Typically, the antenna needs to operate in dual band, one for uplink and one for downlink. The CP rotating sense for each band is opposite to each other to minimize cross-talk. Due to all of these requirements, designing antennas for satellite communications is a challenging task, especially when other constraints such as low profile and low cost are imposed. Furthermore, since the CP rotating sense is opposite, it can be even a more difficult task if the ratio between two operation frequencies is small.

Most of previous planar designs proposed in the literature have utilized conventional or modified microstrip patch arrays. These structures have the disadvantage of using complicated feeding networks. This issue becomes more problematic when dual-band operation with opposite rotating sense is required, which often results in multi-layered structures [1]–[7]. Antennas utilizing metasurfaces [8]–[10],

substrate-integrated waveguide (SIW) [11] or ridge-gap waveguide feed [12] have been proposed as alternatives, however, the complexity in feeding still required multi-layered configurations. Single-layer structures were achieved in [13], [14], but still with a large number of power dividers and matching circuits [13] or with a very narrow bandwidth [14]. Another method is to utilize metasurface-inspired Fabry-Pãl'rot structure [15] in which each unit cell is specifically designed to achieve ±90° phase shift in each band; nevertheless, the structure has high profile and the axial ratio (AR) bandwidth is small.

To achieve high-gain antenna with a simple feeding and a low-profile structure, the concept of leaky-wave antenna (LWA) and series-fed patch array antenna is often utilized. Conventional LWAs and series-fed patch array antennas are one-dimensional (1D) structure fed by a straight transmission line. Two-dimensional (2D) realization of such antennas have recently started to gain more attention from antenna researchers and designers [16], [17] with the potential

of increasing the gain while retaining the advantage of a simple feeding. Several attempts have been made to design dual-band dual-sense CP antenna, however, these designs still required complicated multi-layered feeding structures [18], [19].

This paper demonstrates a passive 2D spiral series-fed patch array antenna that can achieve all aforementioned requirements on a single-layered substrate, using a simple feeding method based on proximity coupling. In particular, the proposed design works as a dual-band dual-sense CP antenna at 12 GHz and 14 GHz, i.e., the frequency bands allocated for satellite communications in Ku-band in Australia. It is also noted that the method presented here can be straightforwardly adapted to other frequencies. The paper is structured as follows. Section II will provide a brief review on linear series-fed patch array antenna for the sake of completeness and to demonstrate the general feeding principle. The main contribution of the paper is shown in Section III and Section IV where single-arm and multi-arm spiral series-fed patch array antennas are analyzed and demonstrated. Measured antenna performance is then shown in Section V, followed by a conclusion.

II. THEORY AND REVIEW OF LINEAR SERIES-FED PATCH ARRAY

We first review the recent 1D series-fed patch array design concepts introduced in [20], [21], which will be exploited to develop the proposed 2D spiral series-fed patch array. This section mainly serves as review of the general physical principle noting that the main contributions of this paper is the AR optimization with an off-center via. This feature has not been shown before in [20], [21].

A. LINEAR SERIES-FED PATCH ANTENNA

Series-fed patch array antennas are conventional structures, which have been demonstrated starting four decades ago [22]–[24]. The series-fed patches are progressively radiating when the electromagnetic power is transmitted along the host transmission line (typically a microstrip line). In this paper, we will focus on the CP realization mechanism where circular patches are fed by proximity coupling [20], in a generic configuration illustrated in Fig. 1(a). This method has two main advantages, namely that the propagation constant β remains nearly the same as that of the feeding microstrip line, and that the leakage rate α_{rad} can be conveniently controlled by varying the gap g between the host microstrip line and the patches. This antenna can be classified as a longitudinally asymmetrical LWA as analyzed in [25]. For this type of antenna, both shunt and series power are radiating with 90° phase difference, resulting in CP radiation. For broadside radiation, the distance between two elements is selected as λ_g where λ_g is the guided-wavelength of the feeding microstrip line. This will ensure that all patches radiate with the same phase (Fig. 1(b)).
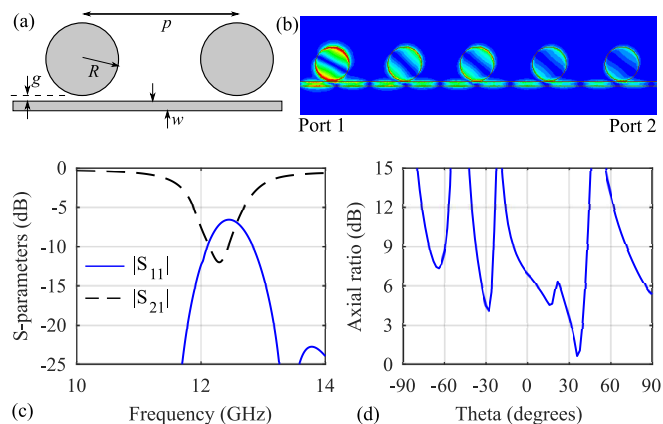

FIGURE 1. (a) A non-optimized series-fed patch array with proximity coupling. (b) Simulated instantaneous E-field distribution at 12 GHz. (c) Simulated S-parameters, (d) Simulated AR at 12 GHz.

Figure 1 shows the S-parameters and AR results of a non-optimized design. The antenna is designed with Rogers TMM-4 substrate ($\epsilon_r = 4.5$, $\tan\delta = 0.002$ and thickness $h_s = 0.762$ mm) with patch elements resonating at $f_1 \approx 12$ GHz (Fig. 1(c)). As shown in Fig. 1(d), the AR is about 6.5 dB at broadside. To obtain a better AR, the authors in [20] added a rectangular slot in the patch center to control the two orthogonal modes in the circular patches. Later, in [21], the slot was rotated to provide more degrees of freedom in optimizing the AR. Nevertheless, it has been found that the slot is not effective when the coupling gap g is large. It is noted that a relatively large value of g is needed when a small coupling is required to achieve higher gain. Therefore, in this paper, we modify the design by replacing the slot by a shorting via in the middle of the patch. Theoretically, a via precisely at the center does not affect the fundamental radiating modes of a circular patch, i.e., two degenerate orthogonal TM_{11} modes. By slightly varying the position of this via to be off-center (in both x- and y-direction), the two orthogonal modes are disturbed and their amplitude ratio and phase can be optimized to improve the AR.

Figure 2 shows the results for an optimized design. It can be noticed that the reflection coefficient has improved as the AR is optimized towards 0 dB by controlling the asymmetry of the structure. This agrees with the analysis in [25] as in this case both shunt and series power radiate with the same magnitude and as a consequence, the antenna efficiency can approach 100% when a sufficient number of series elements is used.

B. DUAL-BAND CONCEPT

To open a second band at a frequency $f_2 > f_1$, another array of smaller circular patches resonating at f_2 is added on the other side of the transmitting microstrip line [21]. Due to the asymmetry, i.e., depending whether the patches are on the left or right of the microstrip line, the rotating sense of these patches are opposite. Since each patch array is only excited in a relatively small bandwidth at the resonance
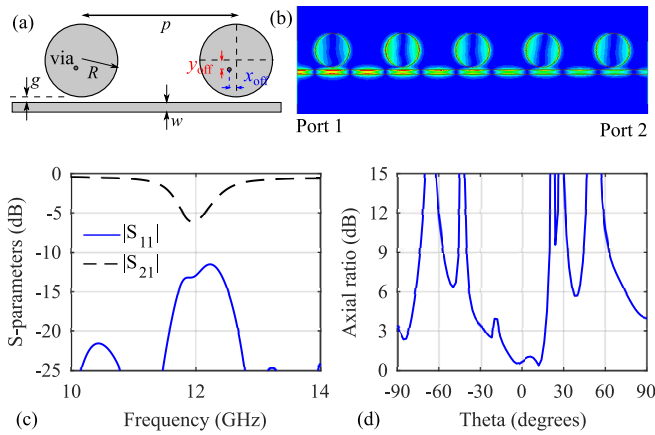
FIGURE 2. (a) A CP series-fed patch array with proximity coupling optimized with off-center vias. (b) Simulated instantaneous E-field distribution at 12 GHz. (c) Simulated S-parameters, (d) Simulated AR at 12 GHz.
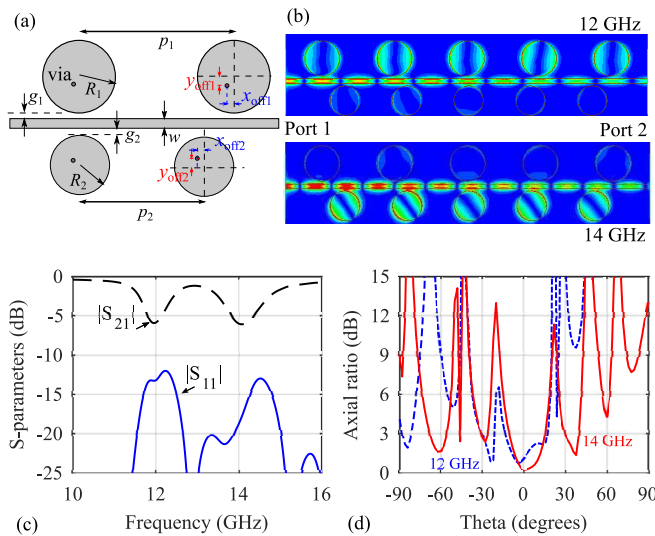

FIGURE 3. (a) A CP dual-band dual-sense series-fed patch array with proximity coupling optimized with off-center vias. (b) Simulated instantaneous E-field distribution at 12 GHz adn 14 GHz. (c) Simulated S-parameters, (d) Simulated AR at 12 and 14 GHz.

frequency f_1 or f_2, they do not significantly affect each other. Thus, this design concept is still working when f_1 and f_2 are quite close to each other. It is noted that when $f_1 = f_2$, the RHCP and LHCP modes are added up, resulting in a linearly polarized antenna. Fig. 3 shows the optimized design and its performance for $f_1 = 12$ GHz and $f_2 = 14$ GHz. The AR is less than 3 dB across the 3 dB-beamwdith at both operating frequencies.

III. SINGLE-ARM SPIRAL SERIES-FED PATCH ANTENNA

In order to increase the gain, more radiating elements need to be added alongside with a reduction in the coupling between the patches and the host transmission line. In a linear arrangement, this results in a very long 1D structure with a fan-beam pattern where frequency-dependent beam squinting can be a serious issue. An array of parallel 1D structures can be designed but it still requires a feeding network with power
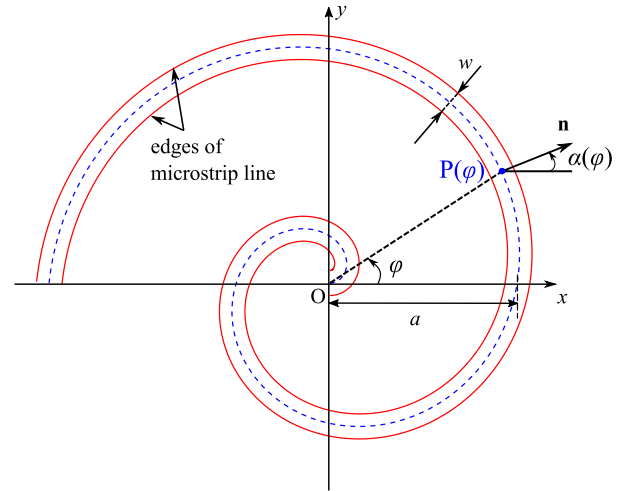

FIGURE 4. Design of spiral microstrip line with constant width w (number of turns $N = 1.5$ in this diagram).

dividers. As an alternative with simple feeding, we propose a spiral series-fed patch array. The concept is to use a uniform microstrip line in a spiral configuration to feed the whole array. In this section, the feeding is demonstrated first, followed by the explanation on how the patches are arranged to obtain broadside radiation. Based on this, a single-arm spiral series-fed patch antenna is designed, followed by a discussion on the radiation efficiency.

A. SPIRAL FEEDING

A conventional Archimedean spiral is utilized for the host transmission line. The parametric equation $P(\varphi) = (x(\varphi), y(\varphi))$ for a spiral starting at the origin in cartersian coordinates is derived as

$$r(\varphi) = \frac{a}{2\pi}\varphi \Rightarrow \begin{cases} x(\varphi) = \frac{a}{2\pi}\varphi\cos\varphi \\ y(\varphi) = \frac{a}{2\pi}\varphi\sin\varphi. \end{cases} \quad (1)$$

In this equation, φ is the azimuth angle that runs from 0 to $N \times 2\pi$ where N is the number of turns (N does not need to be an integer); a is the constant distance between two successive turns (as shown in Fig. 4).

The angle $\alpha(\varphi)$ of the outward normal vector with respect to the x-axis (see Fig. 4) can be derived as

$$\alpha(\varphi) = \arctan\left(-\frac{dx}{dy}\right) = \arctan\left(\frac{-\cos\varphi + \varphi\sin\varphi}{\sin\varphi + \varphi\cos\varphi}\right). \quad (2)$$

It is noted that values of $\alpha(\varphi)$ cover the whole 2π range while the function arctan only yields values in range of $[-\pi/2, -\pi/2]$, so care needs to be taken when performing (3) to ensure $\alpha(\varphi)$ is a continuous function. A more convenient equation to calculate $\alpha(\varphi)$ is

$$\alpha(\varphi) = \begin{cases} \arctan\left(\frac{-\cos\varphi + \varphi\sin\varphi}{\sin\varphi + \varphi\cos\varphi}\right) & \text{if } dy/d\varphi \geq 0 \\ \arctan\left(\frac{-\cos\varphi + \varphi\sin\varphi}{\sin\varphi + \varphi\cos\varphi}\right) + \pi & \text{if } dy/d\varphi < 0. \end{cases} \quad (3)$$

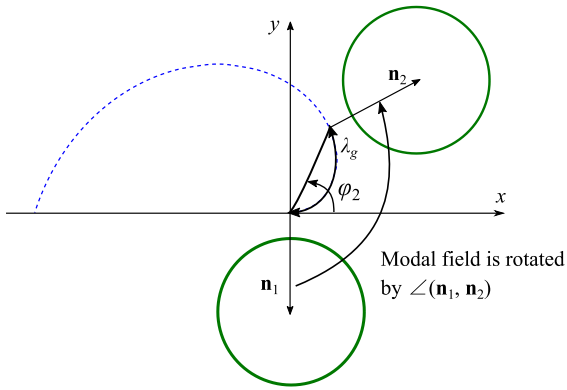The value of $\alpha(\varphi)$ is critical for the patch placement which is shown in the next section.

FIGURE 5. Placement of two patches along a spiral section.

Let the width of the feeding microstrip line be w, the equations for the two edges of the microstrip line can be derived as

$$x(\varphi) = a\varphi \cos \varphi \pm \Delta x(\varphi) \qquad (4)$$
$$y(\varphi) = a\varphi \sin \varphi \pm \Delta y(\varphi), \qquad (5)$$

where

$$\Delta x(\varphi) = \frac{w}{2} \cos \alpha(\varphi) \qquad (6)$$
$$\Delta y(\varphi) = \frac{w}{2} \sin \alpha(\varphi). \qquad (7)$$

Equations (5)-(8) are obtained by "shifting" the original spiral curve along the normal direction at each location by $+w/2$ and $-w/2$. This ensures that the microstrip line maintains its constant width w at any point along the spiral curve (Fig. 4).

The length of the spiral from its center is

$$L(\varphi) = \int_0^\varphi \sqrt{\left(\frac{dx}{d\varphi}\right)^2 + \left(\frac{dy}{d\varphi}\right)^2} \, d\varphi$$
$$= \frac{1}{2}\varphi\sqrt{1+\varphi^2} + \frac{1}{2} \ln \left| \varphi + \sqrt{1+\varphi^2} \right|. \qquad (8)$$

It is noted that this length $L(\varphi)$ is important to calculate the phase delay from the center of the spiral to a position $P(\varphi)$ along the spiral. This phase delay is

$$\varphi_{DL} = L(\varphi)\beta = 2\pi \frac{L(\varphi)}{\lambda_g}, \qquad (9)$$

where β is the propagation constant of the host microstrip line.

B. PATCH PLACEMENT

The patch placement is critical to ensure that all the patches are radiating with uniform phase to obtain broadside radiation. For a linear 1D series-fed patch array, the distance between two patches can be simply selected as λ_g. For a spiral feeding, the radiating phase of the patch is not only affected by the phase delay provided by the microstrip line, but also by curvature of the feeding line defined by $\alpha(\varphi)$.

To understand this, one can consider the simple case shown in Fig. 5. Two patches are placed on the outside

of the microstrip line at position $\varphi_1 = 0$ and φ_2 such that $L(\varphi_2) = \lambda_g$. We choose the radiating phase reference at the first patch $\psi_{r1} = \psi_r(\varphi = 0) = 0°$. Since $L(\varphi_2) = \lambda_g$, the phase of the microstrip line at φ_1 and φ_2 is the same. However, due to the curvature of the microstrip line, the field is rotated by an angle made of the two normal vectors $\mathbf{n}_1$ and $\mathbf{n}_2$. From the definition of $\alpha(\varphi)$, this angle can be calculated as $\alpha(\varphi_2) - \alpha(\varphi_1)$. Therefore, the excitation phase of the second patch is $\psi_{r2} = \alpha(\varphi_2) - \alpha(\varphi_1)$. By this argument, the excitation phase of a patch placed at an arbitrary position $P(\varphi)$ at a distance $L(\varphi)$ from the spiral feed can be found as

$$\psi_r(\varphi) = \alpha(\varphi) - \alpha_0 - \varphi_{DL}$$
$$= \alpha(\varphi) - \alpha_0 - 2\pi \frac{L(\varphi)}{\lambda_g}, \qquad (10)$$

where α_0 is the angle of the normal vector corresponding to the first patch which is used as a phase reference, and φ_{DL} is calculated as in (10).

Physically, (10) implies that to make sure that all of the patches have the same excitation phase, we need to select the location of the patches such that $L(\varphi)$ compensates for the field rotation due to the curvature of the microstrip line.

For the case that the patches are placed on the other side of the microstrip line (for the 2nd band), the normal vector towards the patch is now in the opposite direction. Hence, the excitation phase is

$$\psi_r'(\varphi) = -\alpha(\varphi) - \alpha_0 - \varphi_{DL}$$
$$= -\alpha(\varphi) - \alpha_0 - 2\pi \frac{L(\varphi)}{\lambda_g}. \qquad (11)$$

Using (10) and (11), it is straightforward to select two sets of angles $\{\varphi_i\}$, $\{\varphi_i'\}$ such that the excitation phase $\psi_r(\varphi_i)$ (and $\psi_r'(\varphi_i')$) are the same for all indices i. Furthermore, since α_0 is a constant, it can be ignored when selecting $\{\varphi_i\}$ and $\{\varphi_i'\}$. These two sets correspond to a spiral array of patches on either side of the feeding microstrip line. The analysis here also provides a tool to design the antenna with an arbitrary beam direction rather than broadside, but this is beyond the scope of this paper.

C. PRELIMINARY DESIGN

Using the framework developed in this section, a dual-band dual-sense CP single-arm spiral series-fed patch array has been designed for operation at 12 GHz and 14 GHz as shown in Fig. 6. The parameters for the spiral are $a = 15.3$ mm and $N = 2.125$. The value of a should be chosen large enough to have sufficient space for the patches of both bands, and small enough to avoid grating lobe in the array. Here a is about $0.7\lambda_0$ at $f_2 = 14$ GHz (where λ_0 is the free-space wavelength). Optimized parameters (unit: mm) for this antenna are the microstrip line width $w = 0.8$, radii of the patches $R_1 = 3.27$, $R_2 = 2.75$, location of off-centered vias $x_{off1} = 0.27$, $y_{off1} = 0.56$, $x_{off2} = 0.29$, $y_{off2} = 0.53$, and gap sizes $g_1 = 0.52$, $g_2 = 0.59$. These parameters are defined in Fig. 3(a).
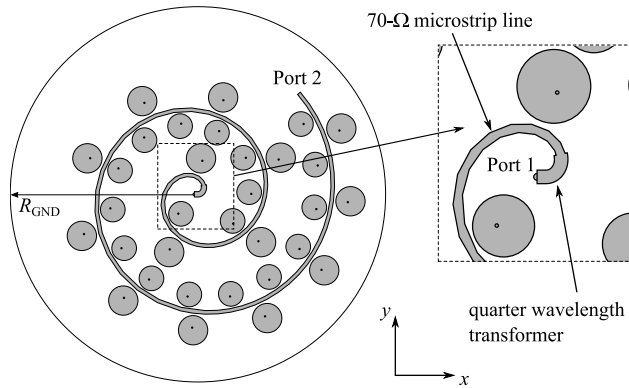
FIGURE 6. Design of a dual-band dual-sense CP antenna with a single-spiral microstrip line. Ground plane size $R_{GND} = 42.5$ mm.
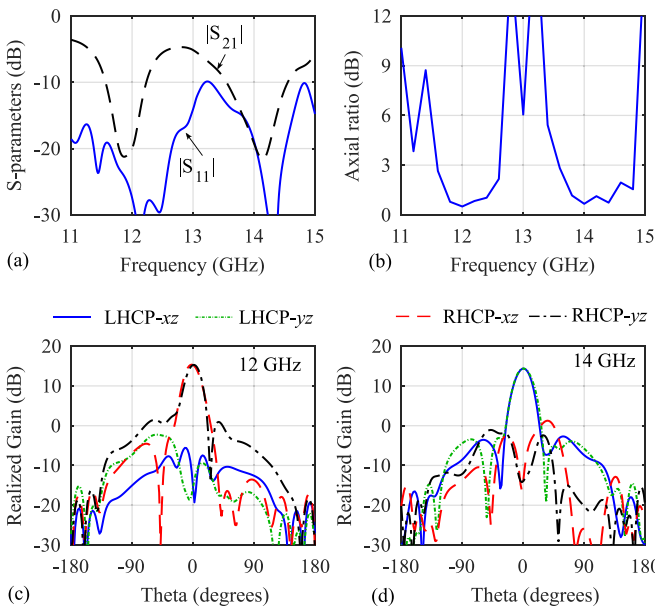

FIGURE 7. Simulated results of the single-arm spiral series-fed patch array in Fig. 6: (a) S-parameters; (b) Axial ratio at broadside versus frequency; (c) Realized gain at 12 GHz; (d) Realized gain at 14 GHz.

The antenna is excited perpendicularly from the bottom by a 50-Ω coaxial connector at the onset of the spiral (Port 1 in Fig. 6). Given a substrate with a fixed thickness (TMM-4, $\epsilon_r = 4.5$ and thickness $h_s = 0.762$ mm), the 50-Ω microstrip line width can be calculated as $w_{50\text{-}\Omega} = 1.5$ mm. However, it is empirically found that a smaller value of w makes the control of the coupling with the patch more convenient. Thus, we choose here $w = 0.8$ mm (which yields a slightly higher characteristic impendance of 70 Ω). In this case, a single quarter-wavelength impedance matching section added at the beginning of the feed is sufficient to achieve good matching to a 50-Ω connector.

The antenna performance is summarized in Fig. 7. The simulated radiation efficiency is 82.1% and 81.5% at 12 GHz and 14 GHz, respectively (both conductor and dielectric losses are taken into account in simulation). The simulated realized gain at broadside reaches 15.3 dBi at 12 GHz and

14.3 dBi at 14 GHz. It is noted that the realized gain should also take the absorption at Port 2 into account (as shown in the next subsection). The slightly higher gain at 12 GHz is due to the fact that the effective aperture for the 12 GHz array is larger than that for 14 GHz since the patches for 14 GHz are placed inside of the spiral (see Fig. 6).

D. ANTENNA EFFICIENCY DISCUSSION

In terms of efficiency, a series-fed patch array antenna can be considered as a LWA, where the radiation efficiency is calculated as

$$\eta_e = \frac{\alpha_{\text{rad}}}{\alpha_c + \alpha_d + \alpha_{\text{rad}}} = \frac{\alpha_{\text{rad}}}{\alpha_{\text{total}}} = 1 - \frac{\alpha_c + \alpha_d}{\alpha_{\text{total}}}. \quad (12)$$

In (12), α_{rad}, α_c and α_d are the leakage rate, the attenuation due to the conductor loss and dielectric loss, respectively. The total antenna efficiency is

$$\eta_{e\text{-total}} = \eta_e \left(1 - |S_{11}|^2 - |S_{21}|^2 \right). \quad (13)$$

Let us assume that the LWA is designed such that P_{term} of power is absorbed at the termination ($P_{\text{term}} = |S_{21}|^2 \approx 1\%$ for the single-arm spiral series-fed patch array in Fig. 6). For a spiral with a total length of L_{total}, the total attenuation constant is calculated as

$$\alpha_{\text{total}} = \frac{\ln(P_{\text{term}})}{-2L_{\text{total}}} \quad (14)$$

Based on this, the leakage rate should be chosen as

$$\alpha_{\text{rad}} = \alpha_{\text{total}} - \alpha_c - \alpha_d. \quad (15)$$

In order to increase the gain, the antenna size, and therefore the spiral length L_{total} need to increase. Thus α_{total} need to be decreased according to (14). Meanwhile, the loss rate of the conductor and substrate (α_c and α_d) stays constant. Therefore, α_{rad} decreases as in (15), which then reduces the antenna efficiency according to (12). As an example, let us attempt to re-design the antenna in Fig. 6 for a higher gain by enlarging the spiral feed with $N = 4$ while keeping $P_{\text{term}} = 0.01$. From the simulation results of the single-arm spiral antenna in Fig. 6, i.e., $\eta_e = 0.821$ with $N = 2.125$ and $a = 15.3$ mm, the sum of conductor and substrate loss is calculated as $\alpha_c + \alpha_d = 1.86$ Np/m. When $N = 4$, the total attenuation rate is calculated from (14) as $\alpha_{\text{total}} = 2.97$ Np/m. Thus, the efficiency is only 37% (about -4.3 dB).

Figure 8 shows the calculated theoretical radiation efficiency for different numbers of turns N for the antenna in Fig. 6. All other parameters remain the same and antenna is designed for fixed $P_{\text{term}} = 0.01$. The result demonstrates that at some point, we cannot increase the gain by making the antenna larger because the radiation efficiency degradation will offset the gain increase through increase of the aperture. Our various simulations indicate that for the considered materials (copper and TMM4 substrate with loss tangent $\tan \delta = 0.002$, thickness 0.762 mm), practically the gain cannot exceed 18 dBic at 12 GHz for a single-spiral feed configuration.
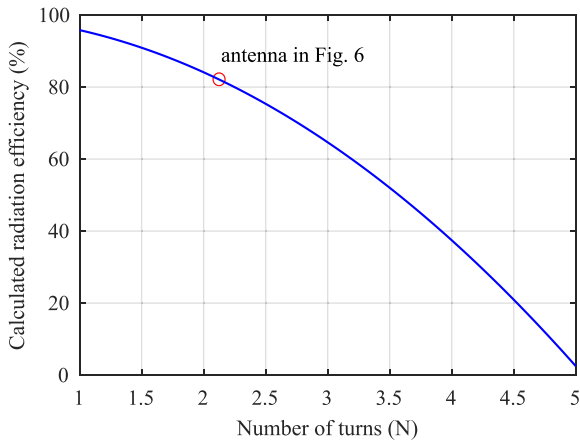
FIGURE 8. Calculated radiation efficiency of the antenna in Fig. 6 designed with different sizes. All other parameters remain the same. P_{term} is fixed at 0.01.

FIGURE 9. Final design of the dual-band dual-sense CP antenna with 4 spiral microstrip line arms.

IV. MULTI-ARM SPIRAL SERIES-FED PATCH ANTENNA

Instead of one spiral arm, N_a number of arms can be used. For the same aperture size, the length of each arm L_{total} is reduced roughly by N_a times. Equations (14) and (15) then infer that the total attenuation constant and leakage rate can be chosen larger. This will result in better radiation efficiency according to (12). Furthermore, using additional spiral arms will result in a more even power distribution in the antenna aperture which will further improves the aperture efficiency and beam radial symmetry.

In general, if the number of spiral arms is larger, a higher antenna efficiency can be achieved. The number of spiral arms is limited by practical considerations on the feeding network at the spiral center. If N_a arms are used and no feeding network is implemented, the impedance of each microstrip line needs to be 50 $\Omega \times N_a$. High value of microstrip line characteristic impedance can result in higher conductor loss and the required thin strips may become difficult to realize. Thus, an impedance matching section is generally needed, which nevertheless is still much simpler than a typical feeding network in a 2D microstrip patch array.

For demonstration, a design with $N_a = 4$ spiral arms is shown in Fig. 9. All parameters for the patches are the same as for the design of single-arm spiral series-fed patch array. The parameters for the spiral are $a = 61.2$ mm and $N = 1$. It is noted that a now is 4 times the value that would be used in a single-arm spiral antenna, which allows to accommodate the 4 intertwined arms. By choosing the value of a in this way, the spacing for the patch placement remains the same. A quarter-wavelength impedance transformer (which is designed at 13 GHz) is used at the center to excite 4 arms of the spiral microstrip line.

If an arm is rotated by an angle α_{arm}, the radiating phase of an element corresponding to that arm is adjusted as

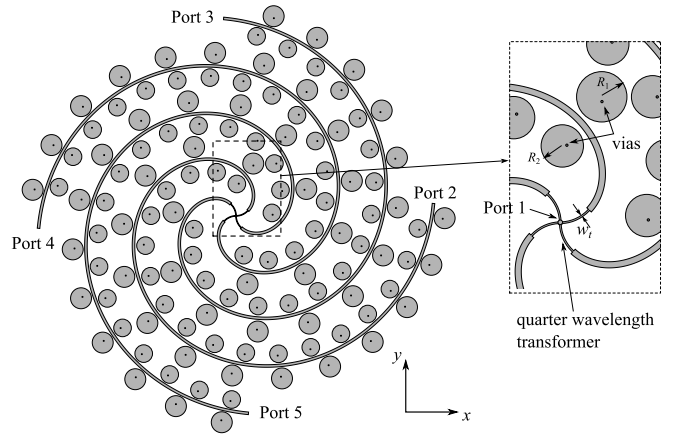$$\psi_{r\text{-rotate}}(\varphi) = \psi_r(\varphi) \pm \alpha_{\text{arm}}, \quad (16)$$

where $\psi_r(\varphi)$ is calculated as in (10) or (11). The above equation is important to ensure that all patches in all arms radiate with the same phase. The $\pm$ sign is selected depending on the side of the patches relatively to the feeding lines. For the case $N_a = 4$, $\alpha_{\text{arm}} = 0°$, $90°$, $180°$ and $270°$.

To avoid reflection at the terminations which can degrade the AR performance, the antenna is terminated with 4 matched ports as shown in Fig. 9. In this case, the relative total power absorbed at all termination is

$$P_{\text{term}} = |S_{21}|^2 + |S_{31}|^2 + |S_{41}|^2 + |S_{51}|^2 \approx 4|S_{21}|^2. \quad (17)$$

One issue with a uniform LWA or series-fed patch array is that the elements closer to the feed radiate with a higher intensity than the elements near the termination. This significantly reduces the aperture efficiency, especially with long structures. This problem is mitigated with the proposed N_a-arm spiral structure since the radiating power can radially spread further, and is therefore distributed more evenly in the aperture. To further improve the aperture efficiency, the gap profile $\{g_{1i}\}$, $\{g_{2i}\}$ can be selected such that the gaps are larger for small i and smaller for large i (i is the element index from the feed to termination). In this design, we choose a simple linear gap profile as

$$g_{1i} = g_{1\text{start}} + (g_{1\text{end}} - g_{1\text{start}})\frac{i-1}{N_1 - 1} \quad (18)$$

$$g_{2i} = g_{2\text{start}} + (g_{2\text{end}} - g_{2\text{start}})\frac{i-1}{N_2 - 1} \quad (19)$$

where $i = 1$ to N_1 in (18) and $i = 1$ to N_2 in (19); N_1 and N_2 are the number of patch elements for the f_1 and f_2-band, respectively. The values for the final design in Fig. 9 are $g_{1\text{start}} = 0.56$ mm, $g_{1\text{end}} = 0.36$ mm, $g_{2\text{start}} = 0.69$ mm, $g_{2\text{end}} = 0.39$ mm. These values are optimized such that $P_{\text{term}} \approx 0.01$ (or equivalently $|S_{21}| \approx -26$ dB) while maximizing the realized gain at broadside for an optimal aperture efficiency.

For demonstration, Fig. 10 shows the simulated electric field distribution at 12 GHz and 14 GHz of the optimized
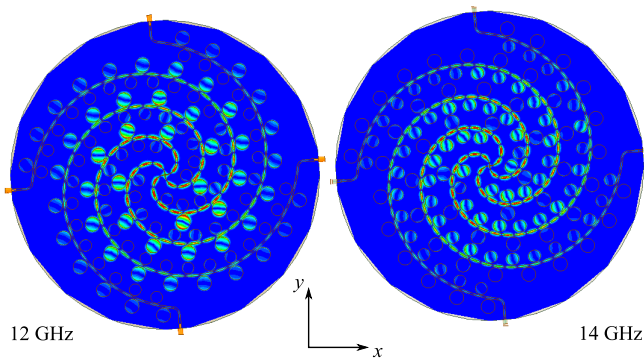
FIGURE 10. Simulated instantaneous electric field at 12 GHz and 14 GHz of the final 4-arm spiral series-fed patch array design.
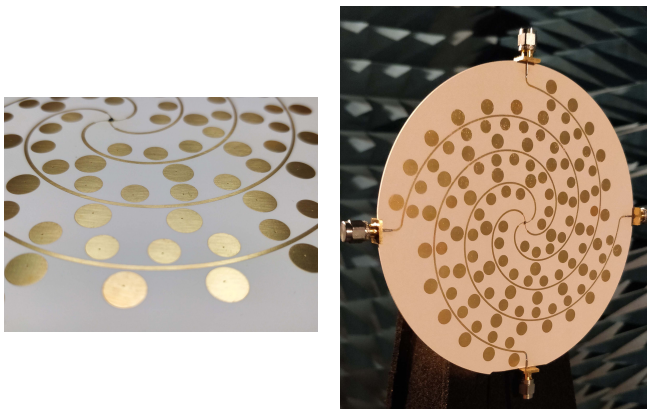

FIGURE 11. Photographs of the fabricated 4-arm spiral series-fed patch array prototype.

FIGURE 12. Simulated and measured S-parameters of the 4-arm spiral series-fed patch array.
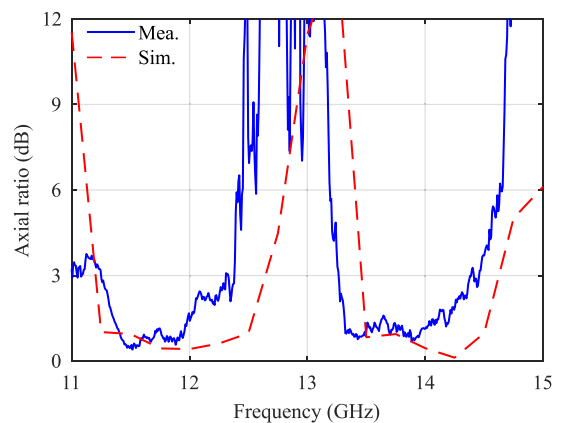
FIGURE 13. Simulated and measured AR at broadside across the frequency.

design. It can be observed that all patches are radiating with almost the same phase, due to the procedure to select the patch positions demonstrated in Section III-B. At each operating frequency, only the corresponding patches are excited. The power is distributed more evenly compared to the previous single-arm design. This results in a more symmetrical radiation pattern and a higher aperture efficiency. It is also noted that there is a small amount of coupling among the patches, however, this coupling does not significantly affect the antenna performance as will be shown in the next section with measurement results.

V. MEASUREMENT

The 4-arm spiral series-fed patch array optimized in Section VI has been fabricated and measured in an in-house anechoic chamber. A photograph of the antenna in its measurement setup is shown in Fig. 11. The simulated and measured S-parameters are shown in Fig. 12. Since $|S_{21}|$, $|S_{31}|$, $|S_{41}|$ and $|S_{51}|$ are similar to each other, only $|S_{11}|$ and $|S_{21}|$ are shown. Both simulated and measured reflection coefficients show good performance in a very wide bandwidth. This is one of the advantage of this type of antennas as impedance matching is relatively simple and robust to achieve compared to conventional patch arrays.
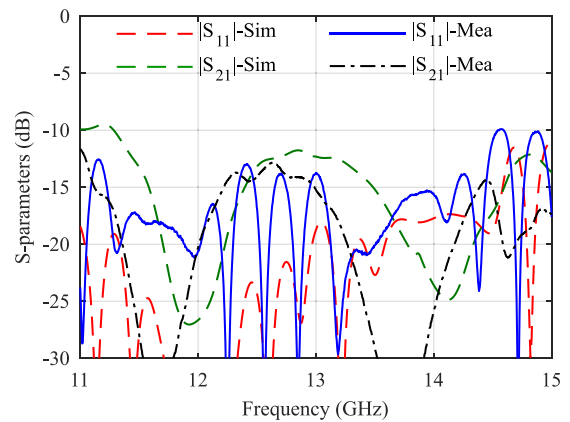
The $|S_{21}|$ results show a slight shift to the left (of about $0.3 - 0.4\%$) for the resonance frequency of the patches. This is mainly due to the tolerance of the substrate material (TMM-4) which may have a slight variation in its relative permittivity. The discrepancy in measured and simulated $|S_{11}|$ can be attributed to the fabrication tolerance at the feed where the quarter-wavelength microstrip line transformer's width is only $w_t = 0.22$ mm (see in the inset in Fig. 9).

Figure 13 shows the simulated and measured AR at broadside across the frequency range. The measured 3-dB AR-bandwidths extend from 11.25 GHz to 12.4 GHz and from 13.25 GHz to 14.4 GHz. Compared to simulation, the measured AR bandwidth is also slightly shifted to the left, which confirms the behavior observed with the measured $|S_{21}|$ parameters. Wide 3-dB AR bandwidths are achieved as about 8% at both bands in both simulation and measurement. At broadside, the measured cross-polarization is lower than -18 dB and -25 dB at 12 and 14 GHz, respectively.

The antenna radiation patterns are shown in Figs. 14 and 15 for 12 GHz and 14 GHz, respectively. The results demonstrate that the antenna exhibits a directive beam at broadside, which confirms that the radiating phase of all patches are close to each other. Dual-sense CP has also
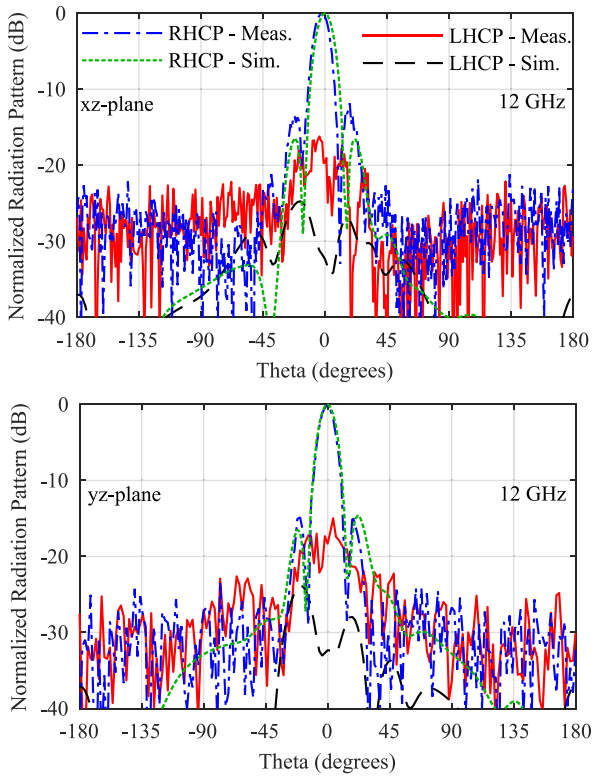
FIGURE 14. Normalized radiation pattern in the *xz*-plane (top) and *yz*-plane (bottom) at 12 GHz. Legends are the same in both figures.
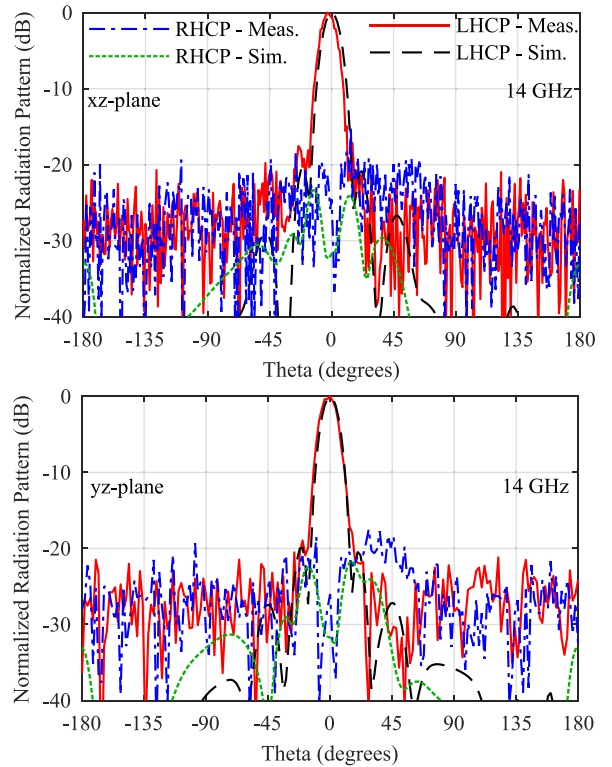

FIGURE 15. Normalized radiation pattern in the *xz*-plane (top) and *yz*-plane (bottom) at 14 GHz. Legends are the same in both figures.

been verified by measurement. The 3-dB beamwidth in both *xz*- and *yz*-planes is about 13°. The ARs as a function of zenith angle θ at 12 GHz and 14 GHz are shown in Fig. 16 with good performance. The measured AR is below 3 dB within the 3-dB beam width. It is noted that due to the slight frequency shift, the performance is indeed better at about 11.8 GHz compared to the target operating frequency 12 GHz (see Fig. 13).

Finally, Fig. 17 shows the simulated and measured realized broadside gains, which agree quite well to each other. The antenna achieves a measured maximum realized gain of about 21.6 dBic and 22.9 dBic at 12 GHz and 14 GHz, respectively (see Fig. 17). The corresponding simulated values are 21.5 dBic and 22.0 dBic. It is noted the AR (Fig. 13) and gain measurement data (Fig. 17) are smoothen using moving average due to standing wave effect between transmitter and receiver. Slightly higher values in peak measured gain can be attributed to this standing wave effect and other errors in gain calibration. Nevertheless, discrepancies of about 1 dB are expected for typical gain measurement tolerances. The 3-dB gain bandwidth is approximately 7% and 5% at the lower and upper bands, respectively. The simulated total efficiency is 81% for both bands. The simulated total efficiency is taking into account both dielectric and conductor loss, as well as the reflection and termination power. Reasonable agreement in the simulated and measured gain indicates a similar value for the practical efficiency of the antenna.
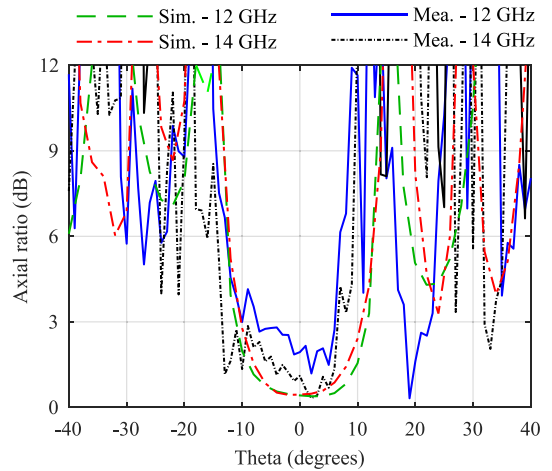

FIGURE 16. Simulated and measured AR versus θ at 12 GHz and 14 GHz.

Finally, Table 1 shows a comparison with other high-gain dual-CP antennas in the literature (λ_0 is the free-space wavelength at the lower band). Only designs with realized gain higher than 13.0 dBi are selected for comparison. It can be seen that the proposed design has a unique structure with unique concept, which makes it low-cost and easy for integration. Only the proposed design and [13] can achieve the functionality with a single-layer substrate. However, [13] stills used complicated feeding network with relatively large element spacing which resulted in higher sidelobe level.

TABLE 1. Performance comparison with literature on High-Gain Dual-CP antennas.

| Work	Design Structure	Feeding	Band	Area (λ_0^2)	Height (λ_0)	Bandwidth (%)	Realized Gain (dBi)
[1]	2D Antenna array, multi-layer	Microstrip line with power divider network	12.0 14.0	2.25	≈ 0.1	13.3 7.4	13.2 13.9
[4]	2D Antenna array, multi-layer	Microstrip line with power divider network	5.3 8.2	3.61	0.08	12.2 12.8	14.5 17.5
[13]	2D Antenna array, single-layer	Microstrip line with power divider network	12.1 17.4	7.54	0.03	9.7 9.8	17.5 18.3
[15]	Fabry Perot antenna, multi-layer	Microstrip patch	7.3 8.0	4.16	0.55	9.7 9.8	13.0 13.3
[18]	Array of stacked patches, 3D structure	Radial line terminated with absorber	12.0 14.0	113	0.28	5.0 4.3	26.0 27.5
Prop.	**Series-fed patches, single-layer**	**Spiral microstrip line**	**12.0 14.0**	**25.9**	**0.03**	**7.1 5.0**	**21.6 22.9**
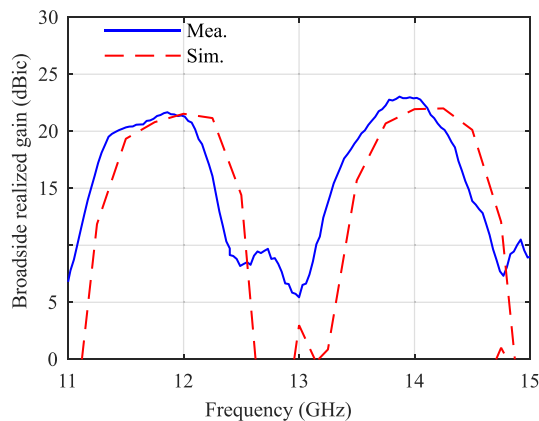
FIGURE 17. Simulated and measured broadside realized gain.

VI. CONCLUSION

In this paper, a theoretical framework for a spiral 2D dual-band dual-sense series-fed patch array with proximity coupling has been developed. Critical aspects of this type of antennas, including feeding, element placement, radiation efficiency and aperture efficiency have been thoroughly discussed. Single-arm and multi-arm spiral series-fed patch arrays were demonstrated with the multi-arm design showing a better performance. A 4-arm spiral series-fed patch array prototype has been validated experimentally, showing an operating bandwidth (overlapped −10-dB impedance bandwidth, 3-dB broadside gain bandwidth and 3-dB AR bandwidth) of 7% at the 12 GHz and 5% at the 14 GHz band. The antenna shows outstanding performance for a single-layered substrate antenna without any external feeding network and with a very low profile of only $0.03\lambda_0$.

REFERENCES

[1] S. Ye, J. Geng, X. Liang, Y. J. Guo, and R. Jin, "A compact dual-band orthogonal circularly polarized antenna array with disparate elements," *IEEE Trans. Antennas Propag.*, vol. 63, no. 4, pp. 1359–1364, Apr. 2015.

[2] A. Garcia-Aguilar, J.-M. Inclan-Alonso, L. Vigil-Herrero, J.-M. Fernandez-Gonzalez, and M. Sierra-Perez, "Low-profile dual circularly polarized antenna array for satellite communications in the x band," *IEEE Trans. Antennas Propag.*, vol. 60, no. 5, pp. 2276–2284, May 2012.

[3] C.-X. Mao, S. Gao, Y. Wang, Q. Luo, and Q.-X. Chu, "A shared-aperture dual-band dual-polarized filtering-antenna-array with improved frequency response," *IEEE Trans. Antennas Propag.*, vol. 65, no. 4, pp. 1836–1844, Apr. 2017.

[4] C.-X. Mao, S. Gao, Y. Wang, Q.-X. Chu, and X.-X. Yang, "Dual-band circularly polarized shared-aperture array for *c* -/ *x* -band satellite communications," *IEEE Trans. Antennas Propag.*, vol. 65, no. 10, pp. 5171–5178, Oct. 2017.

[5] S. Mohammadi-Asl, J. Nourinia, C. Ghobadi, M. Majidzadeh, E. Mostafapour, and A. Haghshenas, "High gain modified dual-band and dual-circularly polarized array antenna," *Wireless Pers. Commun.*, vol. 97, no. 2, pp. 2131–2144, 2017.

[6] M. Wang, D.-Y. Wang, W. Wu, and D.-G. Fang, "Single-layer, dual-port, dual-band, and orthogonal-circularly polarized microstrip antenna array with low frequency ratio," *Wireless Commun. Mobile Comput.*, vol. 2018, pp. 1–10, Apr. 2018.

[7] C.-X. Mao, Z. H. Jiang, D. H. Werner, S. S. Gao, and W. Hong, "Compact self-diplexing dual-band dual-sense circularly polarized array antenna with closely spaced operating frequencies," *IEEE Trans. Antennas Propag.*, vol. 67, no. 7, pp. 4617–4625, Jul. 2019.

[8] K. Li, L. Li, Y.-M. Cai, C. Zhu, and C.-H. Liang, "A novel design of low-profile dual-band circularly polarized antenna with meta-surface," *IEEE Antennas Wireless Propag. Lett.*, vol. 14, pp. 1650–1653, 2015.

[9] J. Zhu, Y. Yang, S. Li, S. Liao, and Q. Xue, "Dual-band dual circularly polarized antenna array using FSS-integrated polarization rotation AMC ground for vehicle satellite communications," *IEEE Trans. Veh. Technol.*, vol. 68, no. 11, pp. 10742–10751, Nov. 2019.

[10] T. Yue, Z. H. Jiang, and D. H. Werner, "A compact metasurface-enabled dual-band dual-circularly polarized antenna loaded with complementary split ring resonators," *IEEE Trans. Antennas Propag.*, vol. 67, no. 2, pp. 794–803, Feb. 2019.

[11] Z.-J. Guo, Z.-C. Hao, H.-Y. Yin, D.-M. Sun, and G. Q. Luo, "Planar shared-aperture array antenna with a high isolation for millimeter-wave low earth orbit satellite communication system," *IEEE Trans. Antennas Propag.*, vol. 69, no. 11, pp. 7582–7592, Nov. 2021.

[12] Y. Liu, Z. Yue, Y. Jia, Y. Xu, and Q. Xue, "Dual-band dual-circularly polarized antenna array with printed ridge gap waveguide," *IEEE Trans. Antennas Propag.*, vol. 69, no. 8, pp. 5118–5123, Aug. 2021.

[13] J.-D. Zhang, W. Wu, and D.-G. Fang, "Dual-band and dual-circularly polarized shared-aperture array antennas with single-layer substrate," *IEEE Trans. Antennas Propag.*, vol. 64, no. 1, pp. 109–116, Jan. 2016.

[14] J.-D. Zhang, L. Zhu, N.-W. Liu, and W. Wu, "Dual-band and dual-circularly polarized single-layer microstrip array based on multiresonant modes," *IEEE Trans. Antennas Propag.*, vol. 65, no. 3, pp. 1428–1433, Mar. 2017.

[15] C. Chen, Z.-G. Liu, H. Wang, and Y. Guo, "Metamaterial-inspired self-polarizing dual-band dual-orthogonal circularly polarized Fabry–Pérot resonator antennas," *IEEE Trans. Antennas Propag.*, vol. 67, no. 2, pp. 1329–1334, Feb. 2019.

[16] M. ElSherbiny, A. E. Fathy, A. Rosen, G. Ayers, and S. M. Perlow, "Holographic antenna concept, analysis, and parameters," *IEEE Trans. Antennas Propag.*, vol. 52, no. 3, pp. 830–839, Mar. 2004.

[17] T. Zhao, D. R. Jackson, J. T. Williams, and A. A. Oliner, "General formulas for 2-D leaky-wave antennas," *IEEE Trans. Antennas Propag.*, vol. 53, no. 11, pp. 3525–3533, Nov. 2005.
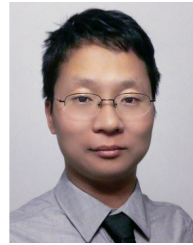
[18] R. Shavit, L. Pazin, Y. Israeli, M. Sigalov, and Y. Leviatan, "Dual frequency and dual circular polarization microstrip nonresonant array pin-fed from a radial line," *IEEE Trans. Antennas Propag.*, vol. 53, no. 12, pp. 3897–3905, Dec. 2005.

[19] K. Wincza and S. Gruszczynski, "Series-fed dual-band dual-polarized antenna lattice fed by slot-coupled power dividers," *IEEE Antennas Wireless Propag. Lett.*, vol. 15, pp. 1065–1068, 2016.

[20] S. J. Chen, C. Fumeaux, Y. Monnai, and W. Withayachumnankul, "Dual circularly polarized series-fed microstrip patch array with coplanar proximity coupling," *IEEE Antennas Wireless Propag. Lett.*, vol. 16, pp. 1500–1503, 2017.

[21] C. D. Bui, N. Nguyen-Trong, and T. K. Nguyen, "A planar dual-band and dual-sense circularly polarized microstrip patch leaky-wave antenna," *IEEE Antennas Wireless Propag. Lett.*, vol. 19, pp. 2162–2166, 2020.

[22] T. Metzler, "Microstrip series arrays," *IEEE Trans. Antennas Propag.*, vol. 29, no. 1, pp. 174–178, Jan. 1981.

[23] D. M. Pozar and D. H. Schaubert, "Comparison of three series fed microstrip array geometries," in *Proc. IEEE Antennas Propag. Soc. Int. Symp.*, vol. 2, 1993, pp. 728–731.

[24] P. Hallbjorner, I. Skarin, K. From, and A. Rydberg, "Circularly polarized traveling-wave array antenna with novel microstrip patch element," *IEEE Antennas Wireless Propag. Lett.*, vol. 6, pp. 572–574, 2007.

[25] S. Otto, Z. Chen, A. Al-Bassam, A. Rennings, K. Solbach, and C. Caloz, "Circular polarization of periodic leaky-wave antennas with axial asymmetry: Theoretical proof and experimental demonstration," *IEEE Trans. Antennas Propag.*, vol. 62, no. 4, pp. 1817–1829, Apr. 2014.

SHENGJIAN JAMMY CHEN (Member, IEEE) received the M.E. and Ph.D. degrees in electrical and electronic engineering from The University of Adelaide, Australia, in 2013 and 2017, respectively.

From 2017 to 2021, he was a Postdoctoral Researcher and a Lecturer with the School of Electrical and Electronic Engineering, The University of Adelaide. He joined the College of Science and Engineering, Flinders University as a Lecturer in 2022. His current research interests include antenna design and engineering, microwave absorbers, and wearable and reconfigurable electromagnetic structures based on novel materials.

Dr. Chen received scholarships, including the Australian Postgraduate Award 2013 and the Simon Rockliff Scholarship 2015. He was also the recipient of a number of awards, including the Young Scientist Best Paper Award at the International Conference on Electromagnetics in Advanced Applications (ICEAA) 2015, the Young Scientist Best Paper Award and Travel Bursary Award at ICEAA 2016, an Honorable Mention at IEEE AP-S Symposium on Antennas and Propagation (APS/URSI) 2017, a CST University Publication Award 2017, and the Best Paper Award at IEEE Asia–Pacific Microwave Conference 2021. He serves as a Reviewer of some prestigious journals, including the IEEE TRANSACTIONS ON ANTENNAS AND PROPAGATION, the IEEE TRANSACTIONS ON MICROWAVE THEORY AND TECHNIQUES, the IEEE ANTENNAS AND WIRELESS PROPAGATION LETTERS, *IET Microwaves, Antennas & Propagation*, IEEE TRANSACTIONS ON BIOMEDICAL CIRCUITS AND SYSTEMS, IEEE ACCESS, and *Electronic Letters*. He was the Chair of the IEEE South Australia Joint Chapter on Microwave Theory and Techniques & Antennas and Propagation from 2019 to 2020.

CHRISTOPHE FUMEAUX (Fellow, IEEE) received the Diploma and Ph.D. degrees in physics from the ETH Zurich, Switzerland, in 1992 and 1997, respectively.

From 1998 to 2000, he was a Postdoctoral Researcher with the School of Optics, University of Central Florida, Orlando. In 2000, he joined the Swiss Federal Office of Metrology, Bern, Switzerland, as a Scientific Staff Member. From 2001 to 2008, he was a Research Associate and a Lecturer with the Laboratory for Electromagnetic Fields and Microwave Electronics, ETH Zurich. Since 2008, he has been with The University of Adelaide, Australia, where he is currently a Professor with the School of Electrical and Electronic Engineering. His main research interests concern electromagnetics, antenna engineering, and the application of RF design principles across the electromagnetic spectrum. He was the recipient of the ETH Medal for his doctoral dissertation, the 2018 Edward E. Altshuler Prize, the 2014 IEEE SENSORS JOURNAL, and the 2004 ACES Journal best paper awards. He also received best conference paper awards at the 2012 Asia–Pacific International Symposium on Electromagnetic Compatibility and the 17th Colloque International sur la Compatibilité Electromagnétique 2014. More than ten of his students have received student awards with joint papers at IEEE conferences. He was the recipient of the University of Adelaide Stephen Cole the Elder Award for Excellence in Higher Degree by Research Supervisory Practice in 2018. From 2011 to 2015, he was a Future Fellow of the Australian Research Council. He served as an Associate Editor for the IEEE TRANSACTIONS ON MICROWAVE THEORY AND TECHNIQUES from 2010 to 2013. From 2013 to 2016, he served as a Senior Associate Editor and later as the Associate Editor-in-Chief for the IEEE TRANSACTIONS ON ANTENNAS AND PROPAGATION. Since March 2017, he has been serving as the Editor-in-Chief for the IEEE ANTENNAS AND WIRELESS PROPAGATION LETTERS.

NGHIA NGUYEN-TRONG (Member, IEEE) received the Ph.D. degree (Doctoral Research Medal) in electrical engineering from The University of Adelaide, Adelaide, SA, Australia, in 2017.

He is currently a Lecturer with The University of Adelaide. His main research interests include microwave circuits, advanced materials, absorbers, and various types of antennas.

Dr. Nguyen-Trong was one of the recipients of the Best Student Paper Award at the 2014 IWAT, the 2015 IEEE MTT-S NEMO, and the 2017 ASA Conferences, and the Best Paper Award at the 2018 and 2020 AMS Conference. He has been continuously selected as a Top Reviewer for IEEE TRANSACTIONS ON ANTENNAS AND PROPAGATION, in 2018, 2019, 2020, and 2021, and IEEE ANTENNA WIRELESS AND PROPAGATION LETTERS, in 2018 and 2021. He serves as a Technical Co-Chair for the 2020 Australian Microwave Symposium (AMS) and 2022 IEEE International Symposium on Antennas and Propagation. He is listed among Australia's Top 40 Early Career Researchers by The Australian, November 2021.